



HAL
open science

Manufacturing of WC-17Co 3D-objects by Laser Powder Bed Fusion followed by heat-treatment

Kevin Papy, Julien Favre, Alexey Sova, Andras Borbely, Philippe Bertrand,
Jean-Marc Staerck

► To cite this version:

Kevin Papy, Julien Favre, Alexey Sova, Andras Borbely, Philippe Bertrand, et al.. Manufacturing of WC-17Co 3D-objects by Laser Powder Bed Fusion followed by heat-treatment. *Matériaux et Techniques*, 2023, 111 (3), pp.304. 10.1051/mattech/2023016 . hal-04145093

HAL Id: hal-04145093

<https://hal.science/hal-04145093>

Submitted on 28 Jun 2023

HAL is a multi-disciplinary open access archive for the deposit and dissemination of scientific research documents, whether they are published or not. The documents may come from teaching and research institutions in France or abroad, or from public or private research centers.

L'archive ouverte pluridisciplinaire **HAL**, est destinée au dépôt et à la diffusion de documents scientifiques de niveau recherche, publiés ou non, émanant des établissements d'enseignement et de recherche français ou étrangers, des laboratoires publics ou privés.

Manufacturing of WC-17Co 3D-objects by Laser Powder Bed Fusion followed by heat-treatment

Kevin Papy^{1,*}, Julien Favre², Alexey Sova¹, Andras Borbely², Philippe Bertrand¹, and Jean-Marc Staerck³

¹ University of Lyon, École Centrale de Lyon – ENISE, LTDS, UMR CNRS 5513, Saint-Étienne, France

² Mines Saint-Étienne, Univ Lyon, CNRS, UMR 5307 LGF, Centre SMS, 42023 Saint-Étienne, France

³ Technogenia, Saint-Jorioz, France

Received: 26 September 2022 / Accepted: 2 May 2023

Abstract. Conventional tungsten carbide (WC) cermet parts containing a cobalt matrix phase are generally produced via powder sintering. In this study it is shown that cermet parts can also be produced by laser powder bed fusion from WC-17Co powder precursor. Optimal process parameters were found for manufacturing without preheated building plate. Micro-structural analysis revealed noteworthy porosity fraction (1.41%) as well as the presence of small-scale cracks in the as-built specimens. It is further shown that most of these defects can be eliminated by heat treatment at ambient pressure or by hot isostatic pressing. Heat treatment also led to the dissolution of the fragile W₂C phase. Hardness test results indicate that the performance of the AM parts was comparable to that of a reference produced via powder sintering. The work is a successful demonstration of manufacturing of cermet parts using laser powder bed fusion.

Keywords: cermet / tungsten carbide / laser powder bed fusion / hot isostatic pressing / hardness

Résumé. Fabrication d'objets 3D à partir de poudre de WC-17Co par procédé de fusion laser sur lit de poudre suivi d'un traitement thermique. Les pièces conventionnelles en carbure de tungstène (WC) contenant un liant cobalt sont généralement produites par procédé de frittage conventionnel. Cette étude montre que les pièces en cermet peuvent également être produites par fusion laser sur lit de poudre à partir de poudre de WC-17Co. Les paramètres optimaux du processus ont été trouvés pour la fabrication sans utilisation de plateau chauffant. L'analyse microstructurale a révélé une fraction de porosité notable (1,41 %) ainsi que la présence de petites fissures dans les spécimens tels que construits. Il est également démontré que la plupart de ces défauts peuvent être éliminés par un traitement thermique à la pression ambiante ou par un pressage isostatique à chaud. Le traitement thermique a également entraîné la dissolution de la phase W₂C fragile. Les résultats des essais de dureté indiquent que les performances des pièces obtenues par procédé de fabrication additive sont comparables à celles produite par frittage conventionnel. Les résultats démontrent la fabrication de pièces de cermet par fusion laser sur lit de poudre.

Mots clés : cermet / carbure de tungstène / fusion laser sur lit de poudre / pressage isostatique à chaud / dureté

1 Introduction

Laser power bed fusion (L-PBF), also known as selective laser melting (SLM), is an additive manufacturing (AM) process used for the production of functional parts with complex shape using a metallic powder as feedstock material. In L-PBF a laser beam melts a powder layer, which after solidification builds up the three-dimensional part layer-by-layer [1–3]. The final physical properties such as roughness, density, porosity, cracking propensity depend on process parameters including the laser power, scanning speed, and powder bed thickness [4–7].

Tungsten carbide/cobalt (WC-Co) cermets are extensively used in the manufacture of cutting tools. The properties and applicability of tungsten alloys depend significantly on the WC content (from 80 to 97 wt.%) as well as the binder phase composition. In general WC-Co cermets exhibit exceptional hardness, low friction coefficients, and high melting points, all of which contribute to a high wear resistance.

WC-Co parts are classically manufactured by powder sintering [8–12]. The layer-by-layer AM method could significantly increase tool design complexity and potentially improve tool performance. Several studies regarding L-PBF manufacturing of WC-Co parts are available in the literature [13–17]. Generally, it is reported that

* e-mail: kevin.papy@ec-lyon.fr

manufacturing good quality parts is challenging due to the high melting point, high thermal conductivity, and brittle nature of the as-built parts. In most cases their integrity was low owing to the presence of long cracks and pores. For example, Uhlmann et al. [18] reported that WC-17Co parts manufactured by L-PBF at low (185 J/mm^3) and high (1667 J/mm^3) energy densities exhibited substantial porosity and cracking. They also established that parameters such as beam focalization, layer thickness, laser power, and scan speed affected the relative density of the WC-17Co material. In contrast to conventional sintering, L-PBF process used laser energy, which lead to a thermal exposure with rapid solidification. This makes the process prone to the formation of pores, cracks and brittle phases with cermet material such as WC-Co. The work provides an interesting optimization study of process parameters, but the possible benefit of post heat-treatment is not explored. Khmyrov et al. [19] used a mixture of WC-75Co and WC-50Co powders to determine the optimal WC content at which cracking can be avoided, mainly caused by the presence of the ternary $\text{Co}_3\text{W}_3\text{C}$ brittle phase. It was found that cracking of AM parts could be avoided only at low percentages of WC, which is not interesting for applications (compared to cermets obtained by sintering). The main objective of the study conducted by Schwaneckamp et al. [20–22] was to reduce the porosity and crack frequency by preheating the support plate. Preheating to 800°C resulted in a significant reduction in crack prevalence and porosity, but a large number of micropores still remained. Further post-treatment by hot isostatic pressing (HIP) resulted in a significant improvement of the material density. The work concluded that the use of a preheated building plate was essential for the successful manufacture of WC-Co parts using L-PBF. The positive effect of HIP reported in their work is encouraging. Therefore, further studies exploring its applicability limits in terms of the microstructure of AM parts could help developing energy efficient methodologies.

Considering the above literature results it can be concluded that L-PBF manufacturing of WC-Co parts remains challenging. Preheating of the building plate to a high temperature allowed the manufacturing of solid samples with some residual porosity that could be eliminated through HIP post-treatment. However, in the absence of a preheating plate the manufacturing of complex-shaped WC-Co parts, even with high internal porosity, was not possible owing to crack formation and to the destruction of the part during cutting from the plate. In addition, it should be confirmed whether the HIP process is able or not to heal the defects formed during AM. Additional information concerning microstructure changes during HIP would be also helpful to understand final physical properties of the manufactured parts.

Present article focuses on the AM of parts using the commercial WC-17Co material and addresses three essential points as illustrated in Figure 1. First, the possibility to produce complex shapes by L-PBF without using a preheated plate will be tested and the optimal process parameters will be determined. In a second step the actual benefits of the HIP post process will be evaluated. Especially a comparison with a

conventional heat treatment will demonstrate the importance of the applied pressure. Finally, the hardness performance of the produced parts will be tested.

2 Material and methods

2.1 L-PBF Equipment

Pro X 200 DMP equipment supplied by 3D Systems was used in the study. The volume of the working chamber where the parts were manufactured was $140 \times 140 \times 125 \text{ mm}^3$. The L-BF machine was equipped with a 400 W fiber laser having a wavelength of 1070 nm. To prevent oxidation the working chamber was filled with nitrogen during manufacturing.

It is important to note that the analysis of the laser beam shape revealed a significant effect on the energy distribution in the beam. In particular, at powers higher than 200 W and long exposure times the energy distribution changed from a Gaussian spot to a ring shape. The energy distribution surfaces measured at laser powers of 130 W and 300 W are presented in Figure 2. Evidently, this shape change significantly complicates the optimization process. To avoid its influence the maximum laser power was limited to 160 W so that the shape of the energy distribution surface remained close to Gaussian. The spot diameter was $130 \mu\text{m}$.

2.2 Powder material

Agglomerated-sintered WC-17Co powder with a particle size distribution of $15\text{--}53 \mu\text{m}$ (Oerlikon Metco) was used in this study. The powder was initially developed for thermal spray applications such as HVOF and HVAF. SEM images of the particles are shown in Figure 3. It is evident that the particles are quasi-spherical in shape.

The average size of the WC grains (dark grey) is in the $1\text{--}5 \mu\text{m}$ range. The carbide grains are uniformly distributed in the cobalt matrix (light grey).

Inductively coupled plasma mass spectrometry (ICP-MS) analysis (see Tab. 1) indicates that the chemical composition was within the range stated by the supplier (C: 4.7–5.5, Co: 14.5–19.5).

X-ray diffraction (XRD) was employed for phase analysis using an X'PertPro MPD diffractometer with $\text{CuK}\alpha$ radiation. Phase quantities were obtained from Rietveld analysis performed with the MAUD software [23]. The powder pattern shown in Figure 4 was fitted with an $\text{Rwp} = 4.1\%$ ($\chi^2 = 3.4$), which resulted in mass fractions of $90 \pm 6\%$ for the WC phase (space group P-6m2) and $10 \pm 4\%$ for the Co phase (space group Fm-3m). The corresponding calculated volume fraction is 0.84% and 0.16% for the WC and Co phases respectively. The phase fraction errors are relatively large, and the results correspond to the lower limit of the nominal composition stated by the manufacturer. The crystallite sizes in the WC and Co phases were 340 and 210 nm, respectively. Additionally, the microstrain in the Co phase was large ($\sim 2 \times 10^{-3}$), whereas it was minimal in the WC phase

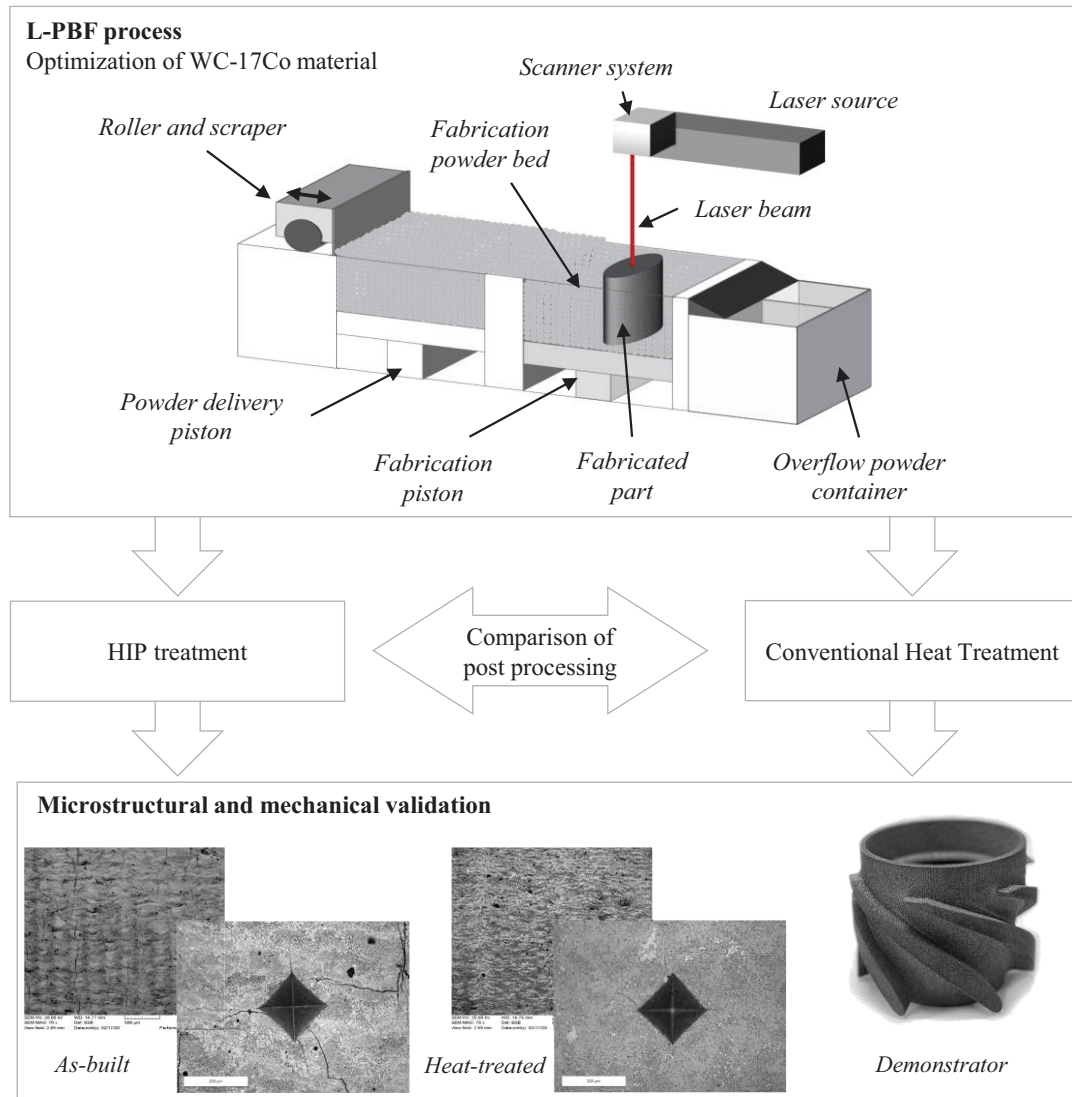


Fig. 1. Global scheme of the study with three main steps: L-PBF process, post heat-treatment and hardness tests.

Fig. 1. Schéma descriptif de l'étude en trois étapes principales : procédé L-PBF, post-traitement thermique et essais de dureté.

($\sim 4 \times 10^{-4}$). The difference between the ICP-MS and XRD results may be related to differences in micro absorption and crystallite size of the two phases.

Various particle properties, such as shape, size distribution, flowability, apparent density and tap density were also analyzed. Powder morphology analysis indicated that the particles were largely spherical with an equivalent diameter of $d_{10} = 24.3 \mu\text{m}$, $d_{50} = 47.8 \mu\text{m}$ and $d_{90} = 73.4 \mu\text{m}$. The powder flowability results were obtained using a Hall flowmeter in accordance with ASTM B527 and ASTM B21, and are presented in Table 2 together with the tap and apparent densities.

2.3 Post-treatment processes

Cube-shaped samples with dimensions of $10 \times 10 \times 10 \text{ mm}^3$ manufactured using L-PBF were used for post-treatment. The first batch of samples was heat-treated (HT) in an oven

at 1450°C under nitrogen atmosphere for 5 h. The second batch was subjected to capsule-free HIP, which is a cycle applied during industrial processes. The HIP process was performed in several steps. First, the temperature was gradually increased from room temperature to 1000°C over 15 h under normal pressure, then it was then elevated to 1450°C at a heating rate of $5^\circ\text{C}/\text{min}$. The furnace was maintained at a pressure of 40 MPa for 5 h. Cooling to room temperature was performed in the HIP chamber at a rate of $6^\circ\text{C}/\text{min}$.

2.4 Structural and mechanical properties

The relative density of the manufactured parts was determined employing the Archimedes method using ASTM-B962 as well as the analysis of scanning electron microscope (SEM) images (using ImageJ [24]). The microstructure and elemental distribution were

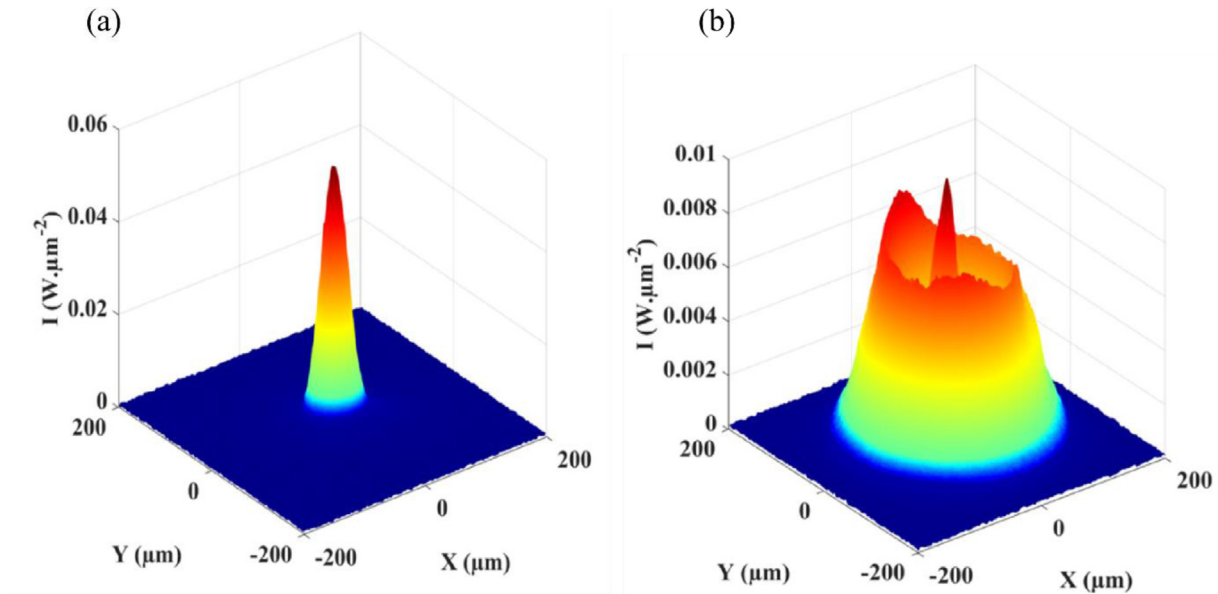


Fig. 2. Intensity distribution surfaces at (a) 130 W and at (b) 300 W (laser power in the focal plane).

Fig. 2. Distribution de l'intensité laser à (a) 130 W et à (b) 300 W (au plan focal).

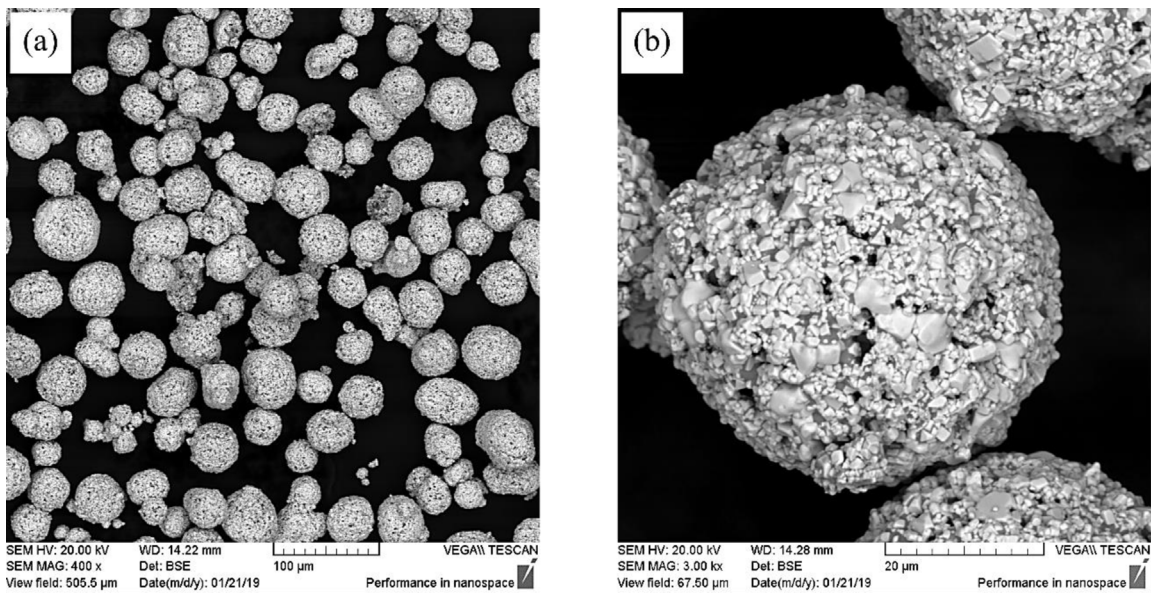


Fig. 3. SEM images of the WC-17Co particles at different magnification (a) x400 and (b) x3000.

Fig. 3. Images MEB de la poudre de WC-17Co suivant différents grossissement (a) x400 et (b) x3000.

Table 1. Chemical analysis of the initial powder according to ICP-MS.

Tableau 1. Analyse chimique de la poudre initiale par procédé ICP-MS.

Element [wt.%]		
W	C	Co
76.4	5.2	18.4

analyzed using a Zeiss Supra 55VP v2 SEM. The mean grain intercept method is a technique used to quantify the grain size of a given material by drawing a set of randomly positioned line segments on the micrograph and then measuring the length of each segment that intersects a grain [24–26]. Vickers hardness (HV) was determined by applying a load of 30 kg for 10 s to all samples. Palmqvist toughness was determined by cracks propagation measurement after indentation test [27,28].

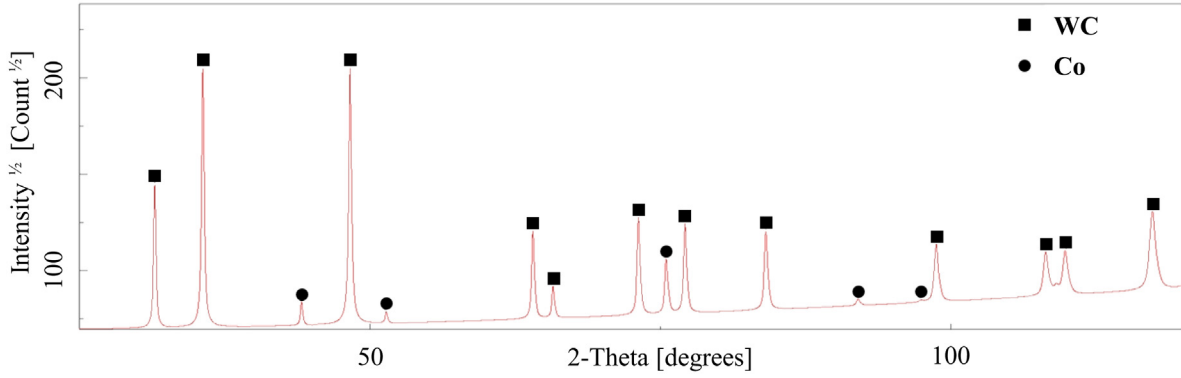


Fig. 4. XRD pattern of the WC-17Co powder used for L-PBF process.

Fig. 4. Diffractogramme de la poudre de WC-17Co utilisée pour le processus L-PBF.

Table 2. Summary of powder properties.

Tableau 2. Résumé des propriétés de la poudre.

Flow rate [s/50 g]	12.4 ± 0.3
Tap density [g/cm^3]	5.9 ± 0.02
Apparent density	5.21 ± 0.03
Hausner index	1.13 ± 0.02
Carr index	11.43 ± 0.02

Table 3. Ranges of L-PBF manufacturing parameters applied in the experiments.

Tableau 3. Plages des paramètres du procédé L-PBF appliqués pour les optimisations paramétriques.

Layer thickness [μm]	30
Range of laser power [W]	100–130–160
Range of scan speed [mm/s]	30–100
Range of hatching distance [μm]	140–200
Inert gas	Nitrogen

3 Results and discussion

3.1 Optimization of process parameters

In the first step, the parametric window of the L-PBF process was determined. The principal purpose of these experiments was to determine the parameters enabling the production of materials with the lowest amount of porosity and cracks. Initially, single tracks were deposited with a powder layer thickness of $30 \mu\text{m}$. The power and scan velocity were varied from 100 to 160 W and from 30 to 200 mm/s, respectively. Table 3 summarizes the parameter ranges tested in the first stage.

Observation of the track shape allowed to conclude that stable tracks were formed only when the scanning speed was in the 30–40 mm/s range at a laser power of 130 W. Following the single-track experiments, 3D objects with simple geometries (cubes and parallelepipeds) were manufactured. Numerous factors can affect the process results, such as the laser power, scan speed, hatch spacing, layer thickness, and scanning strategy. These factors are important because re-melting depends on the amount of the energy density (E_v) absorbed during the process [29], which is defined by the following equation:

$$E_v = \frac{P}{V_s \times Hd \times l}, \quad (1)$$

where E_v is the energy density (J/mm^3), P is the laser power (W), V_s is the scanning speed (mm/s), Hd is the hatch distance (mm) and l is the layer thickness (mm).

Similar approaches based on energy density optimization in the L-PBF process have already been successfully applied several times [30,31]. Furthermore, hexagonal and zigzag scanning strategies were applied to produce WC-Co cubes (Fig. 5).

To analyze porosity and other defects the samples were cut parallel to the building direction. Figure 6 (bottom) shows the relationship between sample density and energy density. The plot in Figure 6 (top) indicates that samples with the higher density (98.9%) were manufactured using an energy input of $602 \text{ J}/\text{mm}^3$ and the hexagonal scanning strategy (Fig. 6b). The samples manufactured at a lower energy density (hexagonal scanning strategy) contained significantly more pores and with larger sizes (Fig. 6a). This dramatic increase in porosity is related to the lack of fusion of the WC-Co powder. An increase in the energy density above $602 \text{ J}/\text{mm}^3$ led to crack formation in addition of lacks of fusion. The samples manufactured at $833 \text{ J}/\text{mm}^3$ using the hexagonal scanning strategy contained more cracks than low E_v and had the lowest density, which indicates a high level of residual stress. The optimum energy density for manufacturing in the zigzag scanning strategy was found to be $560 \text{ J}/\text{mm}^3$. Therefore, due to manufacturing difficulties to produced large part, hexagonal strategy with an optimal E_v of $602 \text{ J}/\text{mm}^3$ was used. For comparison, the optimal E_v level of the Co-28Cr-6Mo alloy is appreciably lower ($\sim 200 \text{ J}/\text{mm}^3$) and its porosity is close to zero [32].

The density of the zig-zag-generated samples was lower than for the hexagonal scanning strategy, therefore, the final batch was produced using the latter. An image of

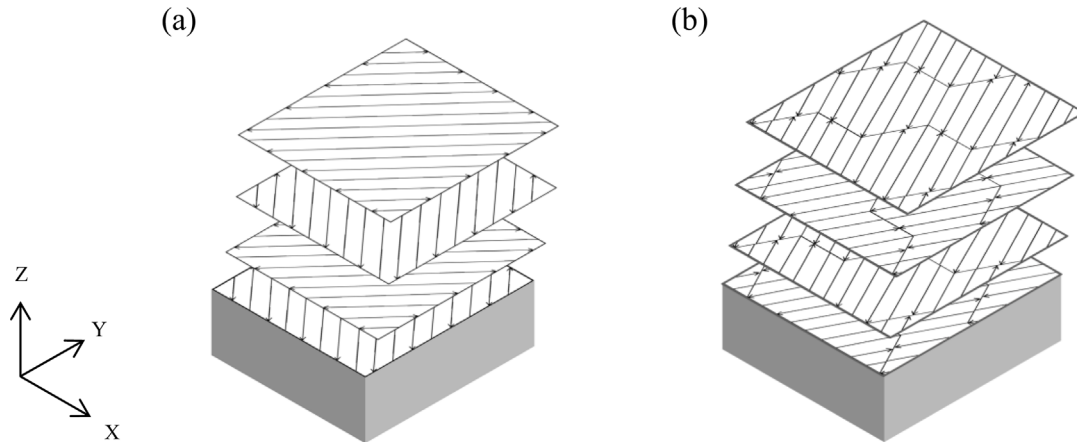


Fig. 5. Schematic illustration of (a) zigzag and (b) hexagonal scanning strategies.

Fig. 5. Illustration schématique des stratégies de balayage (a) en aller/retour et (b) hexagonale.

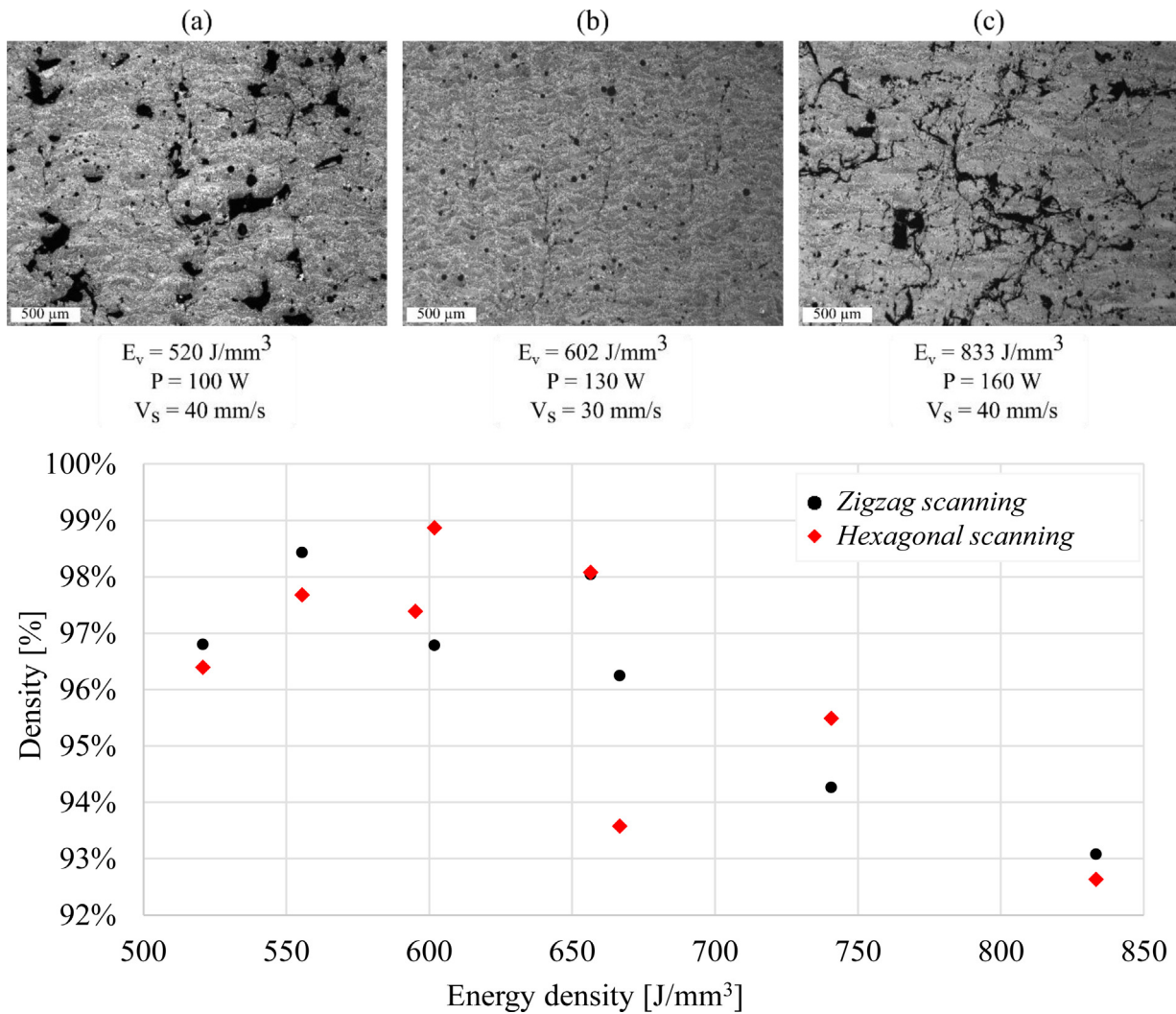


Fig. 6. Top: SEM images of samples manufactured via the hexagonal scanning strategy at (a) low, (b) medium, and (c) high energy densities. Bottom: Plot of sample density vs. energy density for zigzag and hexagonal scanning strategies.

Fig. 6. En haut : images microscopes d'échantillons fabriqués selon la stratégie de balayage hexagonale à (a) faible, (b) moyenne et (c) haute densité d'énergie. En bas : évolution de la densité de l'échantillon en fonction de la densité d'énergie volumique pour les stratégies

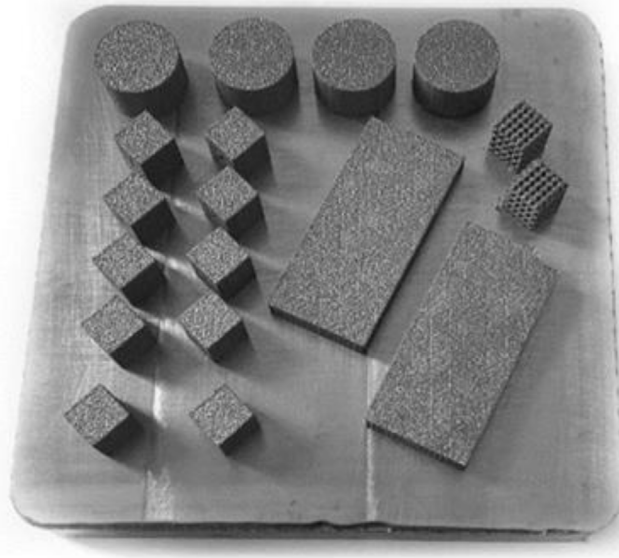


Fig. 7. Image of the building plate and the samples manufactured for various analyses.

Fig. 7. Image d'un plateau d'échantillons fabriqués pour diverses analyses.

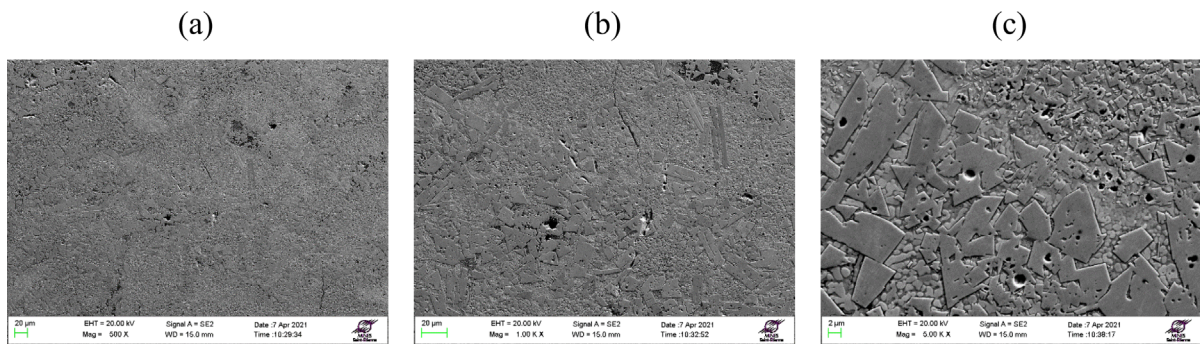


Fig. 8. SEM images of the as-built sample at (a) x500, (b) x1000, and (c) x5000 magnifications.

Fig. 8. Images MEB de l'échantillon brut de fabrication aux grossissements (a) x500, (b) x1000, et (c) x5000.

the building plate and the manufactured samples is shown in [Figure 7](#). Blocks ($50 \times 25 \times 10 \text{ mm}^3$) were built for abrasive wear tests, and cubes ($10 \times 10 \times 10 \text{ mm}^3$) and cylinders ($\text{Ø}20 \times 10 \text{ mm}$) for various characterizations. Lattice-structured cubes were also built to test the limits of manufacturing using cermet powder.

3.2 Microstructure and composition of the as-built samples

SEM images of the as-built sample produced at 602 J/mm^3 , applying the hexagonal manufacturing strategy, are shown in [Figure 8](#).

Microstructure observations revealed that unlike the powder, the as-built samples contained significantly irregular carbide grains size. Due to laser impact, large grain bursts into smaller grains in the material and smaller grain are diffused in the binder [33]. A mean WC grain size of $5.5 \mu\text{m}$ was measured. Some submicron carbide

inclusions were also present in the metal matrix. Short cracks and pores were visible throughout the sample ([Fig. 9](#)), but they did not affect the integrity of the cube.

The pore size distribution evaluated with ImageJ is shown in [Figure 10](#). Ten different micrographs were recorded at randomly selected positions on each cross section using a magnification of x50. Pores with sizes of $< 5 \mu\text{m}$ were uniformly distributed in the sample. Larger pores were present mostly at the interfaces between the connected tracks and layers, indicating that the material was only partially melted in these areas.

The XRD pattern corresponding to the as-built sample is shown in [Figure 11](#). Compared to [Figure 5](#) (containing the WC and Co phases only) complex carbides formed during the L-PBF process are also visible, caused by decarburization phenomena. In particular, the W_2C phase and the ternary $\text{Co}_3\text{W}_3\text{C}$ and $\text{Co}_3\text{W}_9\text{C}_4$ phases were present. These phases have compact hexagonal (P63/mmc), cubic (Fd-3m), and compact hexagonal structures (P63/mmc), respectively.

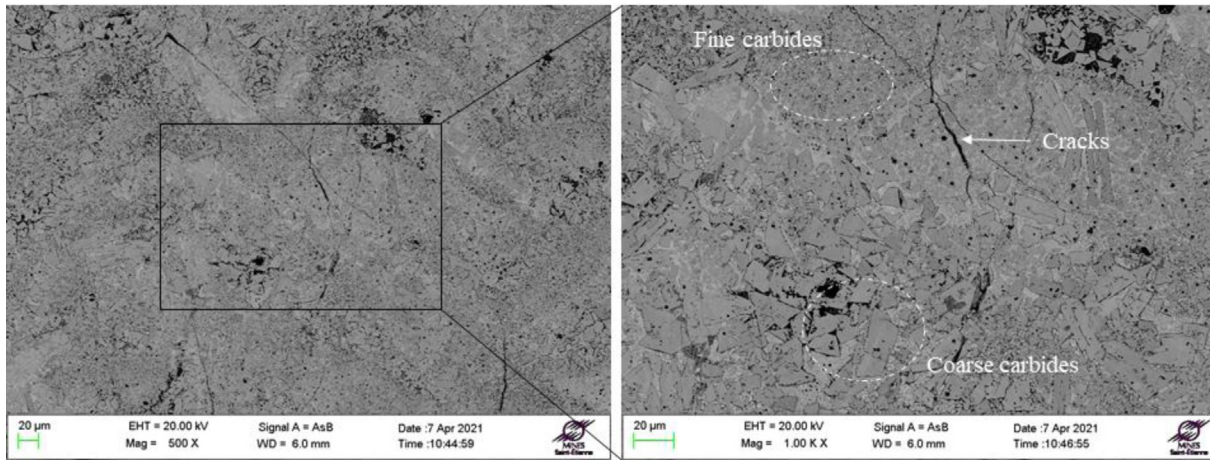


Fig. 9. Secondary electron SEM image of the as-built sample illustrating the presence of cracks, pores, and fine and coarse carbide grains.

Fig. 9. Image MEB de l'échantillon brut de fabrication, illustrant la présence de fissures, de pores et de différentes tailles de grains de carbure.

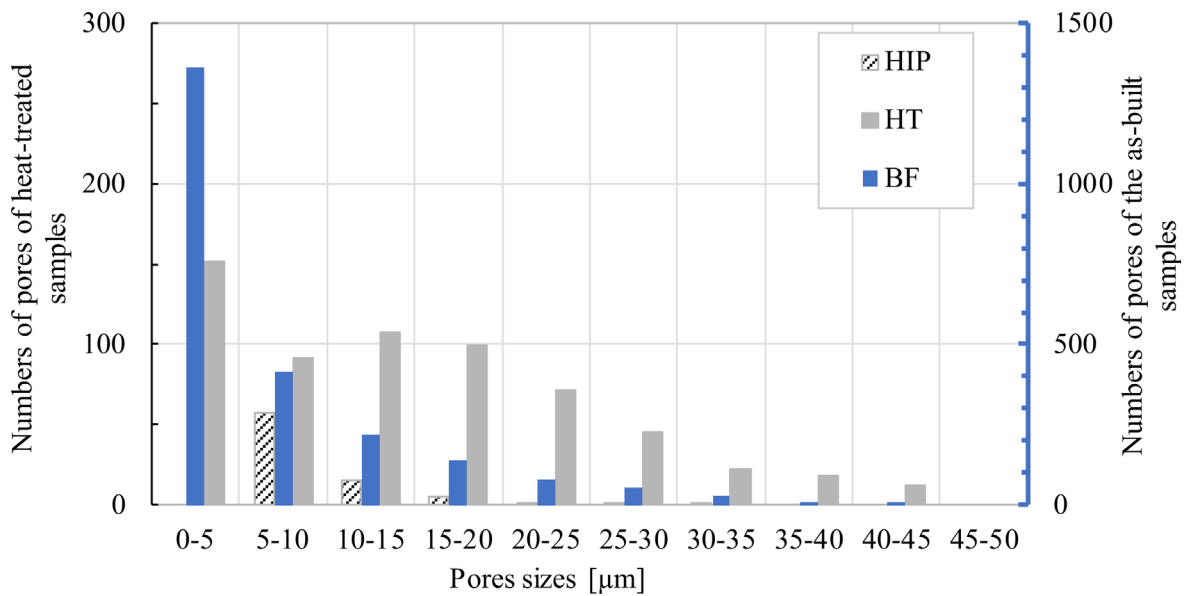


Fig. 10. Pore size distribution in the as-built samples and after heat treatment.

Fig. 10. Distribution de la taille des pores dans les échantillons brut de fabrication et les échantillons après traitements thermique.

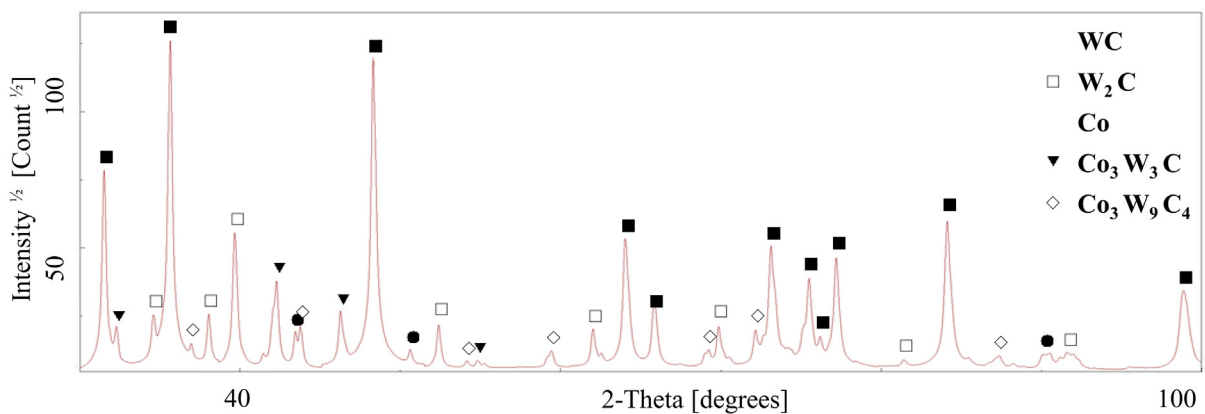


Fig. 11. XRD pattern of the as-built sample.

Fig. 11. Diffractogramme de l'échantillon brut de fabrication.

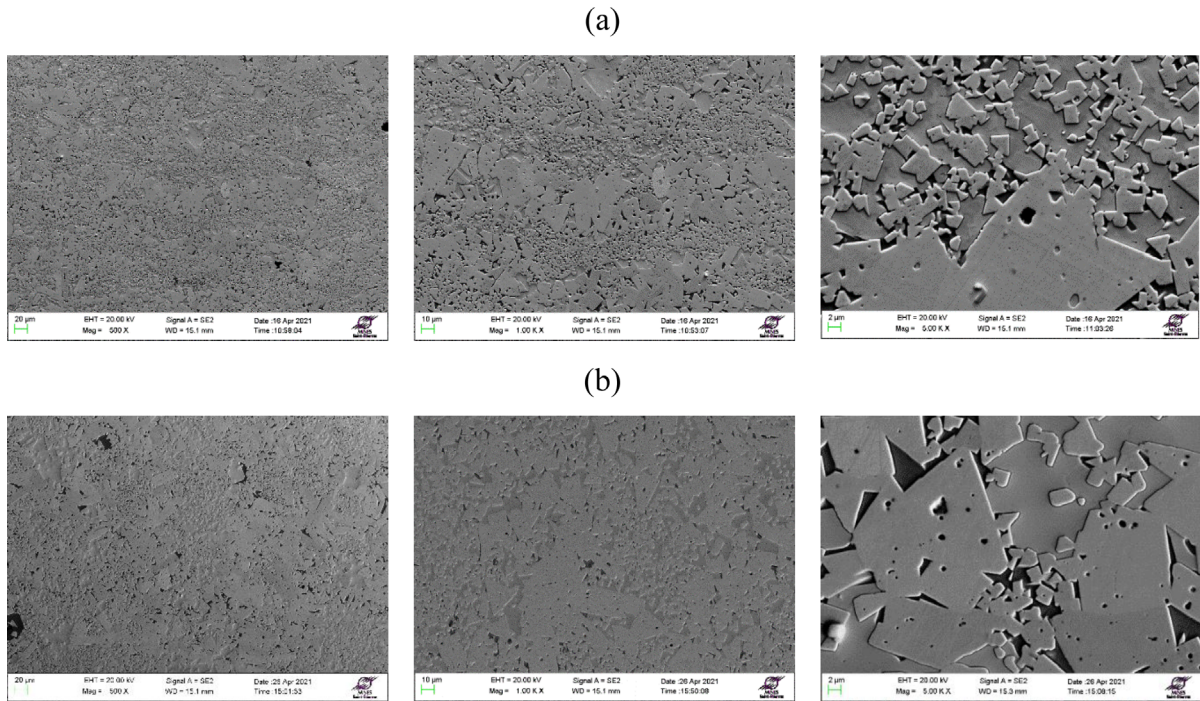


Fig. 12. Sample microstructures after heat treatment at (a) ambient pressure and (b) HIP.

Fig. 12. Microstructures des échantillons après traitement thermique à (a) pression ambiante et (b) HIP.

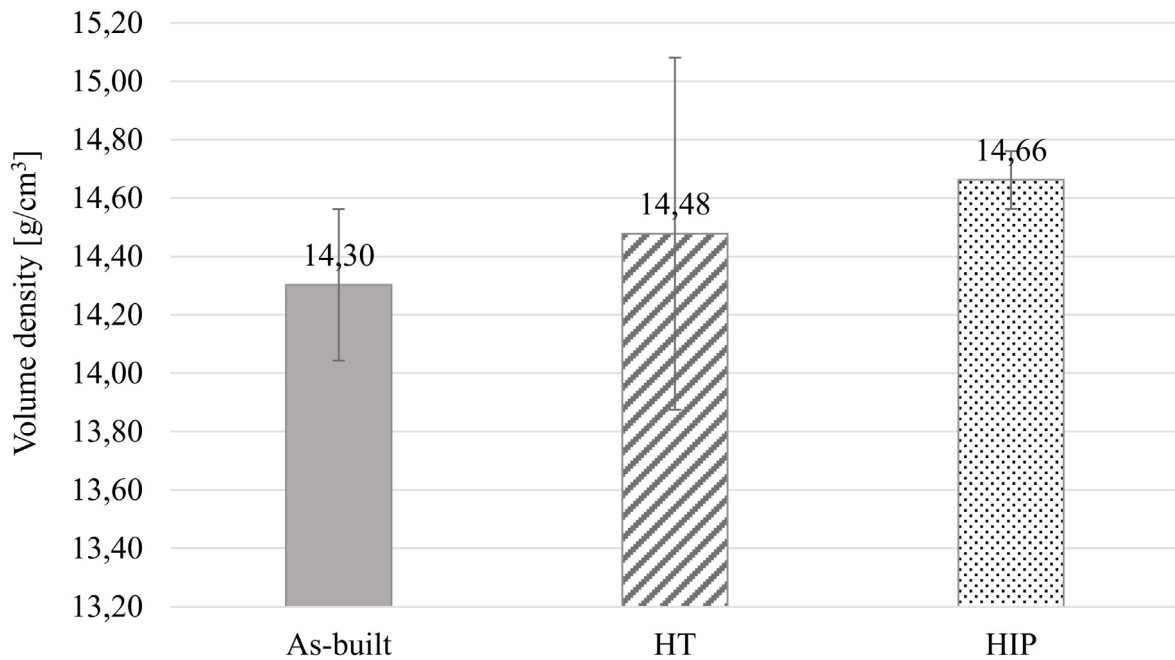


Fig. 13. Mass density results obtained by the Archimedes method for the as-built, HT, and HIP-treated samples.

Fig. 13. Résultats de la densité volumique obtenus par la méthode d'Archimède pour les échantillons brut de fabrication, traité à pression ambiante (HT) et traité par HIP.

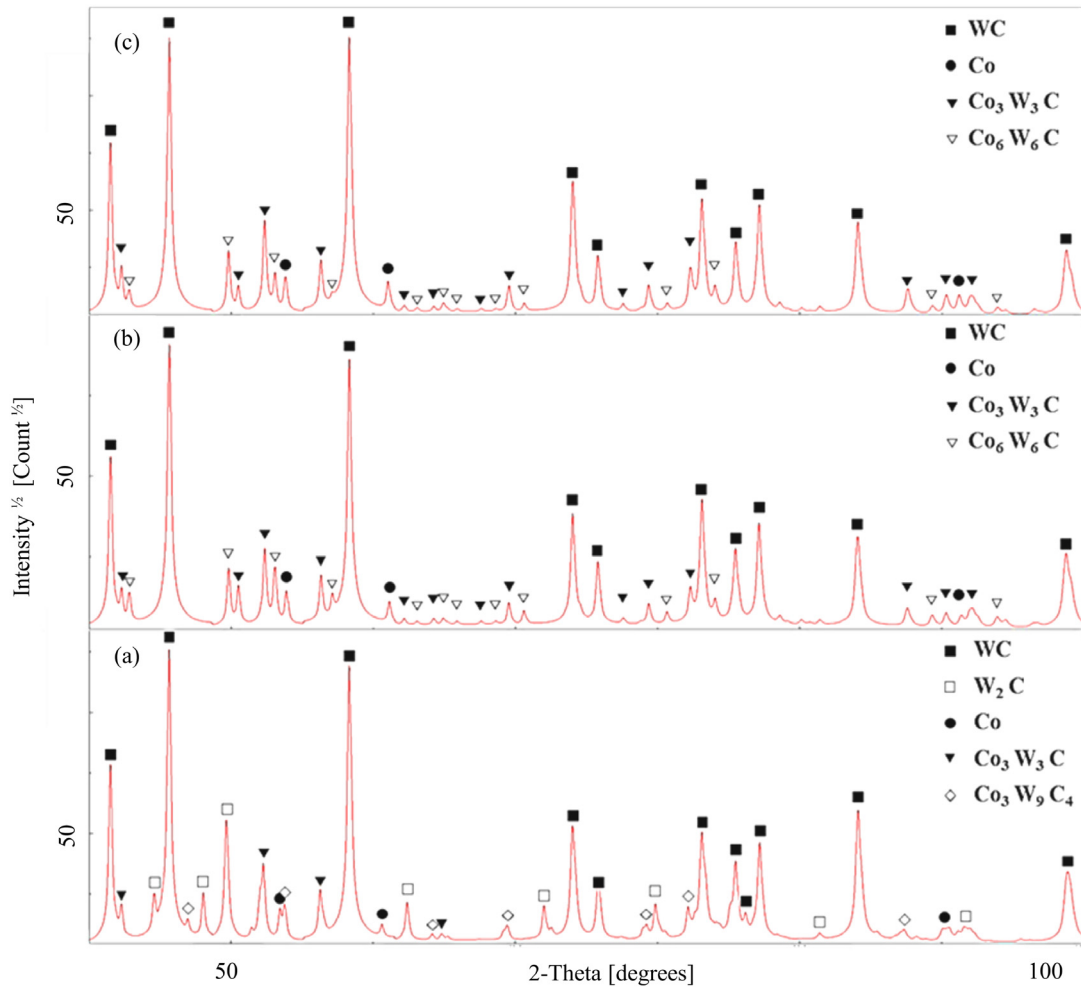


Fig. 14. XRD patterns of the (a) as-built, (b) HT and (c) HIP-treated samples.

Fig. 14. Diffractogramme des échantillons (a) bruts de fabrication, (b) HT et (c) traités par HIP.

Formation of the fragile W_2C and Co_3W_3C phases promote sample cracking during the L-PBF process [34,35]. In conventional powder sintering the W_2C phase is considered undesirable and should be avoided.

3.3 Microstructure and composition of the samples after heat treatment and HIP

Heat treatment of the as-built samples significantly modified their microstructures and crystallographic phases. In particular, cracks were no longer visible (Fig. 12a), because high temperatures promoted material diffusion, allowing for crack closure and sintering of contact surfaces. Carbide grain growth is measured between as-built and heat-treated sample. A mean WC grain size of $8.6 \mu m$ is measured for both heat-treated conditions (Figs. 12a and 12b).

However, heat treatment at ambient pressure had a limited effect on the porosity. According to the image analysis results, the relative density of the HT samples was 98.63%, with the disappearance of many of the smallest pores. In contrast to heat treatment at normal pressure the

Table 4. Results of mechanical test.

Tableau 4. Résultats des essais mécaniques.

Sample	Density [g/cm^3]	HV30
As built	14.30 ± 0.2	1096 ± 45
HT	14.48 ± 0.2	1120 ± 20
HIP	14.77 ± 0.1	1152 ± 17
Sintered reference	14.05 ± 0.1	1160 ± 50

effect of HIP on porosity was remarkable. The microstructure shown in Figure 12b has a mass density of approximately 99.99%. Figure 12 presented before, shows the effect of post-treatment on the pore size and number for all analyzed cases. The apparent density results obtained using the Archimedes method are shown in Figure 13. Four samples were independently analysed for each condition. All measurements were conducted using acetone taking into account the temperature of the fluid. The highest density values were obtained for the HIP-treated samples, confirming the high

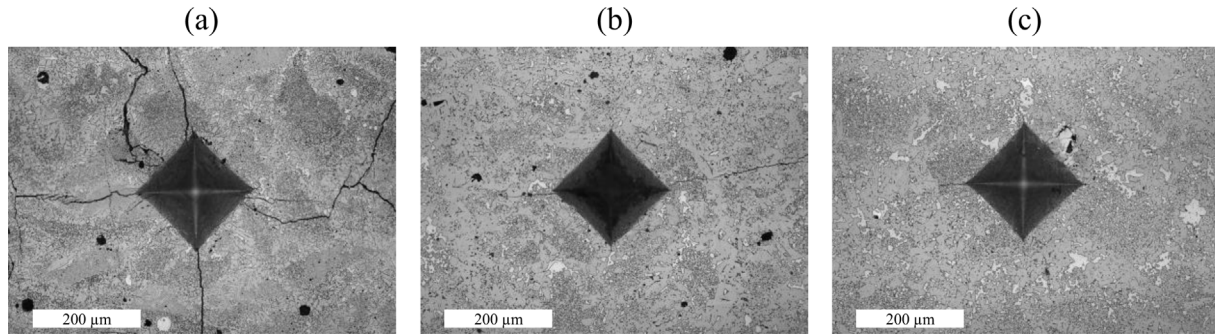


Fig. 15. Overview Vickers indent on the surface of the (a) as-built, (b) HT, and (c) HIP-treated samples.

Fig. 15. Vue d'ensemble de l'empreinte Vickers sur la surface des échantillons (a) bruts de fabrication, (b) HT et (c) traités HIP.

efficiency of this process for pore closure. Nevertheless, the high relative density of 99.99% can also be related to the loss of Co, which might evaporate during L-PBF.

The XRD patterns of the HT and HIP samples presented in Figure 14 are very similar. The phase transformation induced by high-temperature annealing and HIP resulted in the complete dissolution of the fragile W_2C phase, which also has been found in previous studies. Meanwhile, formation of the Co_6W_6C phase with a cubic structure (Fd-3m) was observed in both HT and HIP samples. It can be concluded that the high pressure during HIP treatment did not significantly modify the phase transformation process and that the temperature (1450 °C) during treatments was the key factor influencing the final phase composition.

3.4 Macrohardness Vickers

Macrohardness tests were performed on the as-built, HT, and HIP-treated samples. Three measurements per sample were performed according to the standard methods, and the results are shown in Table 4. The mean value obtained for the as-built samples was 1096 HV_{30} , which is close to those obtained for WC-17Co sintered reference parts [11,36]. In addition, material cracking was observed near the corners of the indent made on the sample cross-section, which indicated high material brittleness (Fig. 15a). The hardness of the HIP-treated (1152 HV_{30}) samples was slightly higher than that of the as-built samples, likely due to their decreased porosity and material integrity improvement. In addition, material cracking was significantly reduced during indentation of the HT and HIP-treated specimens (Figs. 15b and 15c). This result can be related to the absence of the brittle W_2C phase.

The standard deviation of the macrohardness for the HIP and HT samples were lower than those of the as-built samples due to their homogenized structures.

The results of the hardness test and the bulk density of the as-built and heat-treated samples were comparable to the sintered cermet (Tab. 4). This confirmed that the quality of the material produced by L-PBF is sufficiently high to provide suitable applications [11].

4 Conclusion

The feasibility of using L-PBF additive manufacturing without a preheated plate to generate dense cermet samples from WC-17Co was successfully assessed. The results can be summarized as follows:

- the manufacture of dense WC-17Co parts using L-PBF without preheated plate is possible;
- samples with the lowest porosity (1.41%) and highest integrity were obtained using a volume energy density of 602 J/mm^3 and a laser beam power of 130 W. The as-built samples contained the brittle W_2C phase and some small-scale pores and cracks;
- the sample structure, density, and hardness can be significantly improved through capsule-free HIP, resulting in close-to-zero porosity. Heat treatment performed at normal pressure eliminated short cracks and the small-scale porosity and enhanced the material hardness;
- both post-treatment types (at atmospheric pressure and HIP) allowed the dissolution of the undesirable brittle W_2C phase. Other complex carbides, such as Co_3W_3C , $Co_3W_9C_4$, and Co_6W_6C , observed in the as-built samples were also present after simple heat treatment or HIP;
- the macrohardness of the L-PBF-manufactured WC-17Co parts are very close to the values characterizing sintered reference samples;
- the L-PBF parameters defined in this study can potentially be applied for the manufacture of complex-shaped parts of acceptable density and integrity without cracking.

References

1. C.Y. Yap, C.K. Chua, Z.L. Dong, et al., Review of selective laser melting: Materials and applications, *Appl. Phys. Rev.* **2** (4), (2015), <https://doi.org/10.1063/1.4935926>
2. E. Herderick, Additive manufacturing of metals: A review, *Mater. Sci. Technol. Conf. Exhibit.* 2011, MS and T'11 **2** (art. no. 176252), 1413–1425 (2011)

3. N. Li, S. Huang, G. Zhang, et al., Progress in additive manufacturing on new materials: A review, *J. Mater. Sci. Technol.* **35**(2), 242–269 (2019), <https://doi.org/10.1016/j.jmst.2018.09.002>
4. I. Gibson, B. Stucker, D. Rosen, Additive manufacturing technologies 3D printing, in: *Rapid prototyping, and direct digital manufacturing*, 2nd ed., 2019, <https://doi.org/10.1007/978-1-4939-2113-3>
5. C.Y. Zhang, Y.P. Ren, X.S. Chen, The development situation of selective laser melting metal powder based on 3D printing, *Appl. Mech. Mater.* **518**, 12–18 (2014), <https://doi.org/10.4028/www.scientific.net/AMM.518.12>
6. S. Vock, B. Klöden, A. Kirchner, et al., Powders for powder bed fusion: A review, *Progr. Addit. Manuf.* **4**(4), 383–397 (2019), <https://doi.org/10.1007/s40964-019-00078-6>
7. B. Zhang, Y. Li, Q. Bai, Defect formation mechanisms in selective laser melting: A review, *Chin. J. Mech. Eng. (English Ed.)* **30**(3), 515–527 (2017), <https://doi.org/10.1007/s10033-017-0121-5>
8. C. Chen, Z. Guo, S. Li, et al., Microstructure and properties of WC-17Co cermets prepared using different processing routes, *Ceram. Int.* **45**(7), 9203–9210 (2019), <https://doi.org/10.1016/j.ceramint.2019.01.265>
9. Z. Roulon, J.M. Missiaen, S. Lay, Carbide grain growth in cemented carbides sintered with alternative binders, *Int. J. Refract. Metals Hard Mater* **86**(Sep. 2019) 105088 (2020), <https://doi.org/10.1016/j.ijrmhm.2019.105088>
10. H.M. Ortner, P. Eitmayer, H. Kolaska, et al., The history of the technological progress of hardmetals?, *Int. J. Refract. Metals Hard Mater.* **49**(1), 3–8 (2015), <https://doi.org/10.1016/j.ijrmhm.2014.04.016>
11. R.T. Faria, M.F. Rodrigues, I. de Andrade Esquef, et al., On the thermal characterization of a HPHT sintered WC-15%wt Co hardmetal alloy, *Int. J. Refract. Metals Hard Mater.* **23**(2), 115–118 (2005), <https://doi.org/10.1016/j.ijrmhm.2004.11.007>
12. A.S. Kurlov, A.A. Rempel', Effect of sintering temperature on the phase composition and microhardness of WC-8 wt% Co cemented carbide, *Inorgan. Mater.* **43**(6), 602–607 (2007), <https://doi.org/10.1134/S002016850706009X>
13. A. Aramian, S.M.J. Razavi, Z. Sadeghian, et al., A review of additive manufacturing of cermets, *Addit. Manuf.* **33** (Jul. 2019), 101130 (2020), <https://doi.org/10.1016/j.addma.2020.101130>
14. Y. Yang, C. Zhang, D. Wang, et al., Additive manufacturing of WC-Co hardmetals: A review, *Int. J. Adv. Manuf. Technol.* **2020**, 1653–1673 (2020)
15. A. Domashenkov, A. Borbély, I. Smurov, Structural modifications of WC/Co nanophased and conventional powders processed by selective laser melting, *Mater. Manuf. Process.* **32**(1), 93–100 (2017), <https://doi.org/10.1080/10426914.2016.1176195>
16. D. Bricin, A. Kriz, Processability of WC-CO powder mixtures using slm additive technology, *MM Sci. J.* **2019** (June), 2939–2944 (2019), https://doi.org/10.17973/MMSJ2019_06_2018115
17. D. Bricin, Z. Špirit, A. Kříž, Metallographic analysis of the suitability of a WC-Co powder blend for selective laser melting technology, *Mater. Sci. Forum* **919**, 3–9 (2018), <https://doi.org/10.4028/www.scientific.net/MSF.919.3>
18. E. Uhlmann, A. Bergmann, W. Gridin, Investigation on additive manufacturing of tungsten carbide-cobalt by selective laser melting, *Proc. CIRP* **35**, 8–15 (2015), <https://doi.org/10.1016/j.procir.2015.08.060>
19. R.S. Khmyrov, V.A. Safronov, A.V. Gusarov, Obtaining crack-free WC-Co alloys by selective laser melting, *Phys. Proc.* **83**, 874–881 (2016), <https://doi.org/10.1016/j.phpro.2016.08.091>
20. T. Schwanekamp, Parameter study on laser beam melting of WC-Co at 800°C pre-heating temperature, in: *ICAT Proceedings of 7th International Conference on Additive Technologies*, October 2019, pp. 78–84
21. Schwanekamp, Thermal post-treatment of additively manufactured WC-Co processed by Laser Powder Bed Fusion, 2019
22. T. Schwanekamp, M. Reuber, Additive manufacturing of application optimized tungsten carbide precision tools, in: *6th International Conference on Additive Technologies*, January 2016, pp. 100–114, [https://doi.org/10.1016/S0925-8388\(03\)00637-6](https://doi.org/10.1016/S0925-8388(03)00637-6)
23. MAUD, <http://maud.radiographema.eu/>
24. H. Engqvist, B. Uhrenius, Determination of the average grain size of cemented carbides, *Int. J. Refract. Metals Hard Mater.* **21**(1-2), 31–35 (2003), [https://doi.org/10.1016/S0263-4368\(03\)00005-2](https://doi.org/10.1016/S0263-4368(03)00005-2)
25. AFNOR, NF EN ISO 4499 – Métaux durs – Détermination métallographique de la microstructure – Partie 2 : Mesurage de la taille des grains de WC, 2020 (last accessed: Feb. 13, 2023). [Online]. Available from https://viewerbdc.afnor.org/pdf/viewer/rb7Gn_okSoo1?proxy=true
26. S. Luyckx, A. Love, The dependence of the contiguity of WC on Co content and its independence from WC grain size in WC-Co alloys, *Int. J. Refract. Metals Hard Mater.* **24**(1-2), 75–79 (2006), <https://doi.org/10.1016/j.ijrmhm.2005.04.012>
27. Hardmetals – Palmqvist toughness test – ISO 28079, 2009
28. B. Roebuck, E. Bennett, L. Lay, et al., Palmqvist toughness for hard and brittle materials measurement, *Good Practice Guide* **9**, 48 (2008)
29. L.N. Carter, M.M. Attallah, R.C. Reed, Laser powder bed fabrication of nickel-base superalloys: Influence of parameters; characterisation, quantification and mitigation of cracking, 2012
30. J.P. Oliveira, T.G. Santos, R.M. Miranda, Revisiting fundamental welding concepts to improve additive manufacturing: From theory to practice, *Prog. Mater. Sci.* **107**(Jun. 2019), 100590 (2020), <https://doi.org/10.1016/j.pmatsci.2019.100590>
31. K.G. Prashanth, S. Scudino, T. Maity, et al., Is the energy density a reliable parameter for materials synthesis by selective laser melting?, *Mater. Res. Lett.* **5**(6), 386–390 (2017), <https://doi.org/10.1080/21663831.2017.1299808>
32. L. Tonelli, A. Fortunato, L. Ceschini, CoCr alloy processed by selective laser melting (SLM): Effect of laser energy density on microstructure, surface morphology, and hardness, *J. Manuf. Process.* **52**(Oct. 2019), 106–119 (2020), <https://doi.org/10.1016/j.jmapro.2020.01.052>
33. C.J.R.G. Oliver, E.A. Álvarez, J.L. García, Kinetics of densification and grain growth in ultrafine WC-Co composites, *Int. J. Refract. Metals Hard Mater.* **59**, 121–131 (2016), <https://doi.org/10.1016/j.ijrmhm.2016.05.016>
34. R.S. Khmyrov, A.P. Shevchukov, A.V. Gusarov, et al., Phase composition and microstructure of WC-Co alloys obtained by selective laser melting, *Mech. Ind.* **18**(7), (2017), <https://doi.org/10.1051/meca/2017059>

35. H. Ibe, Y. Kato, J. Yamada, et al., Controlling WC/Co two-phase microstructure of cemented carbides additive-manufactured by laser powder bed fusion: Effect of powder composition and post heat-treatment, *Mater. Des.* **210**, 110034 (2021), <https://doi.org/10.1016/j.matdes.2021.110034>
36. Y. Milman, S. Luyckx, I. Northrop, Influence of temperature, grain size and cobalt content on the hardness of WC-Co alloys, *Int. J. Refract. Metals Hard Mater.* **17(1-3)**, 39–44 (1999), [https://doi.org/10.1016/S0263-4368\(98\)00038-9](https://doi.org/10.1016/S0263-4368(98)00038-9)

Cite this article as: Kevin Papy, Julien Favre, Alexey Sova, Andras Borbely, Philippe Bertrand, Jean-Marc Staerck, Manufacturing of WC-17Co 3D-objects by Laser Powder Bed Fusion followed by heat-treatment, *Matériaux & Techniques* **111**, 304 (2023)